

An improved point-to-surface contact algorithm with penalty method for peridynamics

Haoran Zhang^{a,b}, Lisheng Liu^{a,b,*}, Xin Lai^{a,b,*}, Jun Li^{a,b}

^bHubei Key Laboratory of Theory and Application of Advanced Materials Mechanics, Wuhan University of Technology, Wuhan 430070, China

^aDepartment of Engineering Structure and Mechanics, Wuhan University of Technology, Wuhan 430070, China

Highlights

- A point-to-surface contact algorithm applicable to peridynamics is proposed via identifying particles on the outer surface.
- A contact model and an external surface identification model are proposed for peridynamics.
- The identification of external surface particles surpasses the pre-identification of contact surfaces in classical peridynamics.
- The numerical results closely align with the data predicted by classical Hertz theory.

Abstract

It is significantly challenging to obtain accurate contact forces in peridynamics (PD) simulations due to the difficulty of surface particles identification, particularly for complex geometries. Here, an improved point-to-surface contact model is proposed for PD with high accuracy. First, the outer surface is identified using the eigenvalue method and then we construct a Verlet list to identify potential contact particle pairs efficiently. Subsequently, a point-to-surface contact search algorithm is utilized to determine precise contact locations with the penalty function method calculating the contact force. Finally, the accuracy of this point-to-surface contact model is validated through several representative contact examples. The results demonstrate that the point-to-surface contact model can predict contact forces and deformations with high accuracy, aligning well with the classical Hertz contact theory solutions. This work presents a contact model for PD that automatically recognizes external surface particles and accurately calculates the contact force, which provides guidance for the study of multi-body contact as well as complex contact situations.

Keywords: Contact algorithm, Point-to-surface contact algorithm, Penalty function method, Hertz contact theory

1. Introduction

Peridynamics (PD), a non-local theory of solid mechanics, was first proposed in 2000 by Silling [1-3] for discontinuous problems analysis. Unlike traditional continuum mechanics theory, PD uses integral equations instead of partial differential equations to formulate mechanical problems [4]. Owing to the nature of the integral equation, the PD theory adept at studying the mechanical behaviors of structures with cracks or other discontinuities [5]. Meanwhile, a new definition of damage and failure is introduced in the peridynamic theory [6], enabling its spontaneous capability to depict the natural initiation and propagation of cracks. Particularly, PD is a useful tool to study and predict impact behaviors and associated fracture mechanisms due to its advantages in dealing with discontinuities [7]. Notably, the impact-based fracture often involves microscopic cracks, which further develop to macroscopic levels in very short time. Therefore, a series of multi-body collisions and complex contact surface identification problems are involved, However, PD does not have clear surface particle recognition. Thus, it is necessary to propose an accurate and reasonable contact algorithm for complicated contact problems [8].

Generally, impact, extrusion, friction, and closure crack simulations involve complex contact issues [9]. Several methods have been proposed to address the contact problems. In finite element method (FEM) [10-13], Li et al. [14] proposed a cell-based smooth finite element method (CS-FEM) by using the generalized smooth Galerkin weak form of the shape function value, which has certain advantages in dealing with large deformation problems that may lead to mesh deformation. Fang et

al.[15] proposed an improved stable node-based strain smoothing particle finite element method (SNS-PFEM) framework by combining the dual mortar contact method and the dynamic mesh adjustment technique. Through the contact surface smoothing algorithm and small deformation analysis, the undesirable geometric penetration and unbalanced force caused by mesh remeshing were eliminated, respectively. Large deformation contact problems can be modeled more accurately and robustly. Sun et al. [16] proposed a novel node-to-surface (NTS) contact strategy combining the node-based smooth finite element method (NS-FEM) and the edge-based smooth finite element method (ES-FEM) for the 2D frictionless contact problem with triangular elements. The steady-state solution of the static contact problem can be obtained by using an explicit time integration scheme with dynamic relaxation technique. While in mesh-free smoothed particle hydrodynamics (SPH), Libersky's contact algorithm [17] considers general boundary surfaces based on the local smoothing length of smoothed particle hydrodynamics (SPH) particles and offers two options for contact search and force application: particle-surface and particle-particle interactions. Campbell et al. [18] proposed a contact penalty function method suitable for SPH on the basis of considering the contact between particles, only considering the contact between particles, and successfully simulated the process of impact and separation. Zhan et al. [19] developed a hybrid contact algorithm within the SPH framework, combining particle-to-particle and particle-to-segment methods for successful simulations of soil-multibody interaction. Xiao et al. [20] used the surface-to-surface contact algorithm to reconstruct the surface of a three-dimensional object represented by SPH particles, detected the contact between different objects through box detection and cross test, and used the penalty function method to perform contact detection to identify the contact conditions between contact pairs, ultimately achieving successful simulations of high-speed projectile impact on ceramic plates. Although a large amount of research has been focused on contact problems, there is still a lack of efficient and reliable solutions for problems such as rapid identification of new boundaries and accurate calculation of frictional contact forces during the damage process. Aazim et al. [21] used the element-free Galerkin method to study investigates large sliding contact behavior between solid bodies. By discretizing the domain into a set of nodes, all mesh related issues such as mesh distortion, mesh adaption, get eliminated. The node-to-segment technique is used to simulate the large sliding of the contact surface. In particular, as a mesh-free method similar to PD, the SPH method has been successfully applied to address problems involving free-surface flows with fragmentation, some algorithms can detect particles on free surfaces reliably in meshfree method [22, 23]. The discrete element method (DEM) can also examine the mechanical behaviors of discontinuous media, reflecting the movement procedure of multiple deformable bodies [24]. However, the above contact algorithms are mainly based on the contact algorithms with the continuum mechanics framework rather than non-local theory in PD.

In the PD theory, a contact-collision algorithm is proposed to describe rigid and mutable bodies [25], where the impactor is a rigid body and the deformable target material is governed by the PD equations of motion. After contact takes place between the impactor and target material, the material points inside the impactor are relocated to their new positions outside the impactor. This algorithm has been widely used to describe contact collision problems [26-28]. However, the above contact algorithm is only applicable to the contact problem when the body of the impactor is a rigid body and the target plate is a deformable body. When the body of the impactor is a deformable body (e.g., the impactor is a metal), the most commonly used contact model for mutable bodies was proposed by Macek and Silling [29], where a short-range force is defined to prevent material particles from penetrating each other [30-33]. Furthermore, the PD has been coupled with the FEM with the existing dynamic contact algorithm in the FEM for contact calculations [34]. The presence of frictional contact during contact can also affect the accuracy of simulation results. Thus, understanding the frictional contact behavior plays a significant role in predicting the material response in many applications. The friction effect during contact can be considered by applying a pair of frictions perpendicular to the direction of the bond between the particles of the contact material [35] or parallel to the direction of the contact plane [36]. The frictional effect can also be account for by applying a pair of external forces parallel to the bond based on a predetermined relative slip plane [37, 38]. However, the above contact algorithms are

difficult in identifying the contact surface in advance, especially for the particles on the outer surface. Overall, the existing contact model without considering the contact surface cannot analyze the normal forces accurately, while the contact models considering the contact surface is difficult in identifying the contact surface [39]. Notably, due to the lack of pre-identification of contact surfaces in PD, it is almost impossible to accurately pre-identify the contact points, which leads to the problem of ambiguous contact force. Furthermore, to provide guidance on the problem of determining contact surfaces for subsequent studies of contact problems involving frictional effects. Thus, it is essential to develop an improved point-to-surface contact model for describing contact surface and calculating the contact force accurately.

In the present study, without considering friction, a modified point-to-surface contact model with penalty is proposed to address the contact surface problem in advance and calculate the contact force accurately. Based on the assumption that the contact problems only occur on the outer surface of the model, we first identify the model's outer surface using the eigenvalue method. Then, we establish a Verlet list for a simple global search of outer surface particles that may come into contact. Next, a point-to-surface contact search algorithm is employed to analyze the detailed positional information of the contact pairs with a penalty method computing the contact forces for contact pairs. Finally, the contact model is validated with several representative contact examples. The predicted contact forces and deformations exhibit good agreement with the classical Hertz contact theory solutions.

2. Methodology

2.1. Basic Equations of Peridynamics

PD theory is a nonlocal theory proposed by Silling [1-3]. It utilizes spatial integral equations applicable to discontinuous bodies. PD can be primarily divided into two categories: bond-based PD (BB-PD) [1, 6] and state-based PD (SB-PD) [2, 3]. In BB-PD, each material point interacts with points within its neighborhood. The interactions between two material points are called "bonds." Each bond is independent and has a pair of bond forces that are collinear and opposite in direction. Unlike BB-PD, the state-based model incorporates an infinite-dimensional array of information regarding PD interactions. It elucidates how indirect interactions between particles influence other particles.

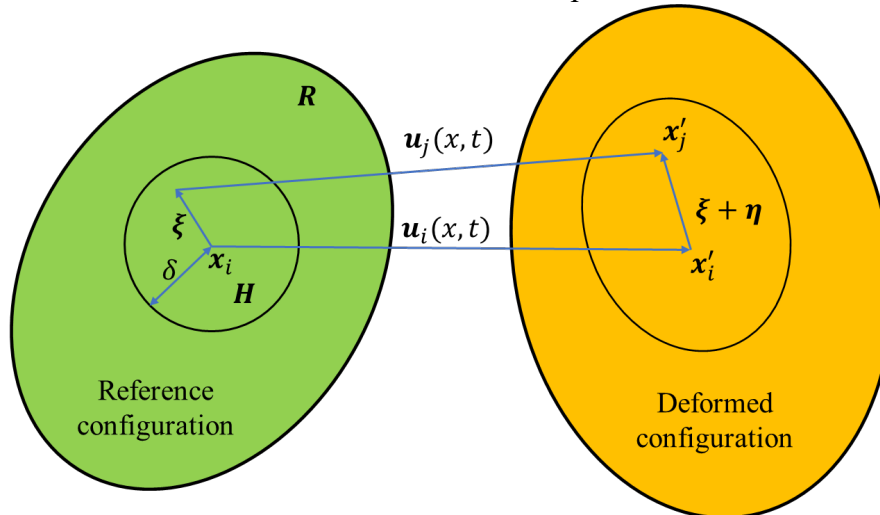


Fig.1. The deformation of a PD bond.

In BB-PD theory, a body occupies a spatial domain, which is considered to be composed of a series of discrete material points ($i = 1, 2, \dots$) and their interacting bonds. As shown in Fig. 1. x_i and x_j represent the position of material points i and j before deformation, respectively, whereas x'_i and x'_j represent the position of material points i and j after deformation. The relative position and relative displacement between material points i and j are denoted by ξ and η , respectively, and

are defined as follows:

$$\boldsymbol{\xi} = \mathbf{x}_j - \mathbf{x}_i, \boldsymbol{\eta} = \mathbf{u}(\mathbf{x}_j, t) - \mathbf{u}(\mathbf{x}_i, t) \quad (1)$$

where, $\mathbf{u}(\mathbf{x}_i, t)$ is the displacement vector field of particles \mathbf{x}_i at time t . Within the spatial domain, any material point i interacts with any other material point j within a finite distance δ . Which makes up a Horizon (\mathbf{H}) of material points i . There is an interaction force between points i and j , which is called the constitutive force function \mathbf{f} . The constitutive force function contains the constitutive information of the material point.

At any time t , the equation of motion for any material point i inside the body in the BB-PD theory is given by:

$$\rho_{x_i} \ddot{\mathbf{u}}(\mathbf{x}_i, t) = \int_{\mathbf{H}_{x_i}} \mathbf{f}(\boldsymbol{\xi}, \boldsymbol{\eta}) dV_{x_j} + \mathbf{b}(\mathbf{x}_i, t) \quad (2)$$

where:

- ρ_{x_i} is the material density of particle i ;
- $\ddot{\mathbf{u}}(\mathbf{x}_i, t)$ is the acceleration vector field of particles \mathbf{x}_i at time t ;
- $\mathbf{f}(\boldsymbol{\xi}, \boldsymbol{\eta})$ is the bond force between particles \mathbf{x}_i and \mathbf{x}_j at time t ;
- $\mathbf{b}(\mathbf{x}_i, t)$ is the external body force density at particles \mathbf{x}_i at time t ;
- \mathbf{H} is the horizon of particle i .

$$\mathbf{H} = \mathbf{H}(\mathbf{x}_i, \delta): \{\mathbf{x}_j \in R: \|\mathbf{x}_j - \mathbf{x}_i\| \leq \delta\} \quad (3)$$

The left term of the equation of motion Eq. (2) represents the resultant force of the material point. In contrast, the integral term on the right-hand side represents the bond force of all material points in the horizon of the material point i . The external body force term is also included on the right-hand side. The entire equation satisfies Newton's second law.

In BB-PD, the essence of the solution is the iterative calculation of the interaction force $\mathbf{f}(\boldsymbol{\xi}, \boldsymbol{\eta})$ between material points and particles within their neighborhood horizon based on time steps. $\mathbf{f}(\boldsymbol{\xi}, \boldsymbol{\eta})$ is obtained based on the selected material constitutive calculation. In the present study, the contact problem between an elastic body and a rigid body is considered, so the bond force expression for the bond-based elastic constitutive model is:

$$\mathbf{f}(\boldsymbol{\xi}, \boldsymbol{\eta}) = cs\mathbf{n} \quad (4)$$

In the equation, $\mathbf{f}(\boldsymbol{\xi}, \boldsymbol{\eta})$ is the bond force vector function, $\mathbf{n} = (\boldsymbol{\xi} + \boldsymbol{\eta})/|\boldsymbol{\xi} + \boldsymbol{\eta}|$ is the normal unit vector of the bond pair after deformation, s is the relative stretch of the bond, and c is the micro-elastic modulus of the object [6]. The specific expression is as follows:

$$c = \frac{6E}{\pi\delta^4(1-2\nu)}, \nu = \frac{1}{4} \quad (5)$$

In the equation, E represents the elastic modulus of the material, δ represents the size of the neighborhood horizon, and ν represents the Poisson's ratio of the material.

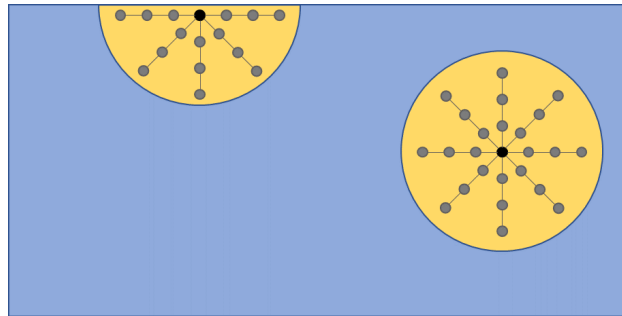


Fig.2. Incomplete neighborhood near the boundary.

Notably, the PD interactions parameters are computed under the assumption that the PD points are in bulk and have complete neighborhood volumes. However, the neighborhood is not complete when the particle is near a boundary, as shown in Fig. 2. If we use the parameters computed for the bulk at points near a material surface, the effective behavior of the PD material model behaves slightly different from the bulk. This is called the PD surface effect [40]. The surface correction is calculated by numerically integrating both dilatation and strain energy density at each material point inside the body for simple loading conditions and comparing them to their counterparts obtained from classical continuum mechanics [25, 41]. For the simple loading condition, the body is subjected to uniaxial stretch loadings in the x -, y - and z -directions of the global coordinate system. The displacement field at the material point \mathbf{x}_i resulting from this loading can be expressed as

$$\begin{aligned}\mathbf{u}_1^T(\mathbf{x}_i) &= \left\{ \frac{\partial u_x^*}{\partial x} x \quad 0 \quad 0 \right\} \\ \mathbf{u}_2^T(\mathbf{x}_i) &= \left\{ 0 \quad \frac{\partial u_y^*}{\partial y} y \quad 0 \right\} \\ \mathbf{u}_3^T(\mathbf{x}_i) &= \left\{ 0 \quad 0 \quad \frac{\partial u_z^*}{\partial z} z \right\}\end{aligned}\quad (6)$$

The displacement gradient is denoted $\partial u / \partial \alpha = \xi$, with $\alpha = x, y, z$. Due to these applied displacement fields, the PD strain energy density at the material point \mathbf{x}_i can be obtained as

$$W_\alpha^{PD}(\mathbf{x}_i) = \frac{1}{4} \sum_{j=1}^N c s^2 |\xi| dV_{x_j} \quad (\alpha = x, y, z) \quad (7)$$

Under simple loading, the strain energy density can be computed by using classical continuum mechanics as

$$W_\alpha^{CCM} = \frac{9E\varepsilon_{\alpha\alpha}^2}{16} \quad (\alpha = x, y, z) \quad (8)$$

With these expressions, a vector of correction factors for the integral terms in dilatation and strain energy density at the material point \mathbf{x}_i can be written as

$$\mathbf{g}(\mathbf{x}_i) = \{g_x, g_y, g_z\}^T = \{W_x^{CCM}/W_x^{PD}, W_y^{CCM}/W_y^{PD}, W_z^{CCM}/W_z^{PD}\}^T \quad (9)$$

Then these correction factors are used as the principal values of an ellipsoid, as shown in Fig. 3, to approximate the surface correction factor in any direction.

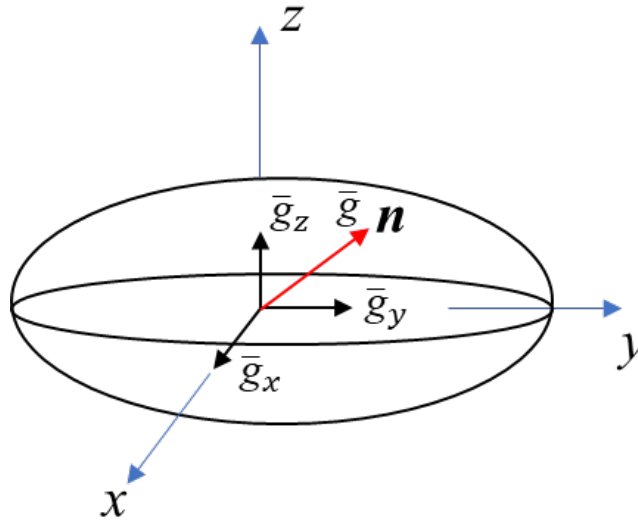


Fig.3. Construction of an ellipsoid for surface correction factors.

Since the mesh density (the gap between the material points) affects the accuracy of the PD

calculations, wherein the effect increases with the increase of grid size and decreases with the increase of neighborhood horizon range. we artificially introduces the transition region of the neighborhood horizon range [42] and defines a volume correction factor v_{ic} . In the case of 3D, the expression of the correction factor is as follows:

$$v_{ic} = \begin{cases} (\delta + r - \|\xi_{ij}\|)/2r \\ 1.0 \end{cases} \quad (10)$$

where $r = \Delta/2$, Δ is the mesh size, $\|\xi_{ij}\| = |x_j - x_i|$.

2.2. Peridynamic Contact Model

Contact-collision algorithms can handle the interactions between any number of objects. Particularly, the contact between multiple objects can be reduced to the pairwise interactions between objects. In general, the mathematical description is given for the contact between two objects without loss of generality. In contact-collision problems, the contact surface cannot be determined in advance and always changes dynamically with time. Therefore, the calculation of contact force mainly involves two aspects: contact search and contact constraint enforcement, in which the determination of the contact interface is the most critical. Contact search is usually divided into two steps: global search and local search. The purpose of global search is to find potential contact pairs, and the purpose of local search is to further accurately determine the real contact state of the contact pairs based on the global search. If a pair is found to be in contact during the local search process, the calculation of the contact force is required for this pair.

2.2.1. Searching for surface particles

In the PD method, the object surface is not directly available. To develop a point-to-surface contact algorithm, it is necessary to obtain the object's surface. To achieve this, we employ the common eigenvalue method [43, 23] to determine the surface particles in the PD model.

First, we use the eigenvalues of the renormalization matrix [17], which is defined as:

$$B(x_i) = [\sum_j \nabla W_{ij} \otimes \mathbf{r}_{ij} \Delta V_j]^{-1} \quad (11)$$

where, $\mathbf{r}_{ij} = x_i - x_j$, ΔV_j is the volume of the j th nearest neighbor particle of particle i , and W_{ij} is the improved Gaussian kernel function [44], as follows:

$$W_{ij} = W(x_i - x_j, h) = \begin{cases} \alpha_d \left[\frac{e^{-(r/h)^2 - c_0}}{1 - c_1} \right] & \text{if } r \leq 3h \\ 0 & \text{otherwise} \end{cases} \quad (12)$$

$$c_0 = e^{-9}; c_1 = 10c_0 \quad (13)$$

$$\alpha_d = \begin{cases} \frac{1}{(\pi^{1/2}h)} & 1-D \\ \frac{1}{(\pi h^2)} & 2-D \\ \frac{1}{(\pi^{3/2}h^3)} & 3-D \end{cases} \quad (14)$$

where, $r = |x_i - x_j|$, h is the grid size (Δ) of particle i . The value of the minimum eigenvalue λ of the matrix \mathbf{B}^{-1} depends on the spatial organization of the particle j near the particle i under consideration. The eigenvalue λ theoretically tends to 0 when the point of matter is far from the surface of the object, while λ theoretically tends to 1 when inside the object. Therefore, we can identify whether the material point is located at the surface of the model according to the value of the least eigenvalue λ of the matrix \mathbf{B}^{-1} . As shown in the following equation, when the value of the minimum eigenvalue λ is greater than 0.75, the material particle i is considered to be an internal particle; Otherwise, the material point i is the particle on the surface [43, 23]. After determining the

particles on the surface, the outer normal direction of the particles on the outer surface is calculated by Eq. (16).

$$\begin{cases} \lambda \leq 0.75 \Leftrightarrow i \in \text{outside} \\ \lambda > 0.75 \Leftrightarrow i \in \text{inside} \end{cases} \quad (15)$$

$$\mathbf{n}(\mathbf{x}_i) = \frac{\mathbf{v}(\mathbf{x}_i)}{|\mathbf{v}(\mathbf{x}_i)|}; \quad \mathbf{v}(\mathbf{x}_i) = -\mathbf{B}(\mathbf{x}_i) \sum_j \nabla W_{ij} \Delta V_j \quad (16)$$

2.2.2. Contact Neighbor List for Particles

To find potential contact pairs, we build a Verlet neighbor list [45, 46], as shown in Fig. 4. With particle i as the center, the potential cutoff sphere with its radius $\delta_{cut} = \Delta$, a skin is added to the outside of the cutoff sphere with a radius of $\delta_m = 1.3\Delta$. The thickness of the skin is $\delta_l = \delta_m - \delta_{cut} = 0.3\Delta$.

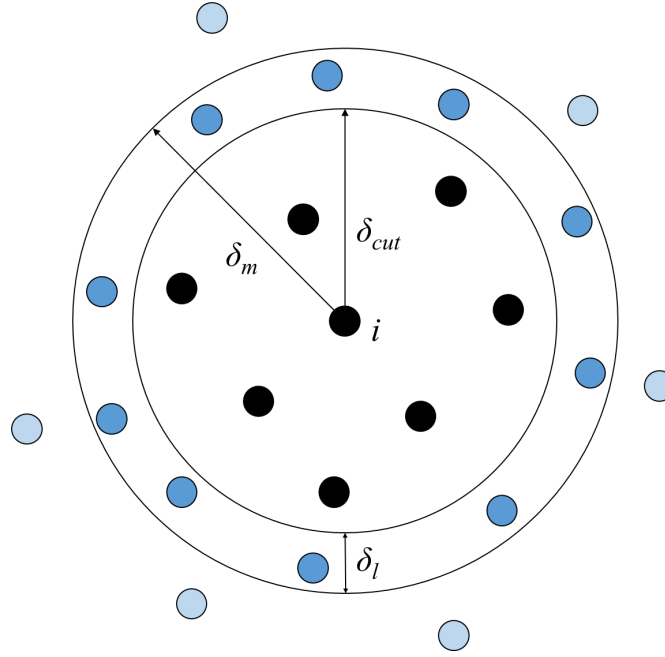


Fig.4. The schematic diagram of the cutoff sphere.

The original Verlet neighbor list is constructed by nested loops over all particles in the system and is completed once every N_m time step. The value of N_m satisfies $\delta_m - \delta_{cut} > N_m \bar{v} \Delta t$, where \bar{v} is the particle velocity and Δt is the time step. The update interval of the original Verlet neighbor list is fixed, regardless of whether the particles move fast enough. Therefore, this generally waste much computational time for larger-scale PD calculations. Therefore, it is necessary to refine the Verlet neighbor list to allow appropriate updates as needed.

This is achieved by maintaining a list of the maximum displacement among all particles after each update of the Verlet neighbor list [47]:

The following steps are taken to implement the algorithm:

1. A list Δs_i is constructed to store the accumulated displacement vector of particle i since the last Verlet list update;
2. In each time loop, Δs_i is updated as $\Delta s_i = \Delta s_i + \Delta u_i$, where Δu_i is the displacement of particle i within each time step loop;
3. The two largest values of particle displacement are calculated and denoted as Δs_{max} and Δs_{max2} ;
4. Before the end of each time step, the values of Δs_{max} and Δs_{max2} are compared with the value of δ_l ;
5. If the sum of the two largest particle displacements $\Delta s_{max} + \Delta s_{max2} > \delta_l$, the Verlet neighbor

list is updated and the accumulated particle displacement Δs_i is reset to zero for the next Verlet neighbor list update.

2.2.3. Point-to-Surface Contact Algorithm

After constructing the Verlet neighbor list, we use the point-to-surface contact algorithm [34, 48] to determine the detailed position information of each potential contact test pair. Since, contact can only occur on the outer surface of an object, and the Verlet neighbor list is constructed for all particles in the model. we establish a contact neighbor list for the surface based on the surface particles to improve the computational efficiency. The list of contact neighbors on the surface can be represented as:

$$CN_f(A) = CN_n(i) \cup CN_n(j) \cup CN_n(k) \cup CN_n(l) \quad (17)$$

where, $CN_f(A)$ is the contact neighbor list of surface A ; $CN_n(a)$, ($a = i, j, k, l$) is the contact neighbor list of points that make up the surface A .

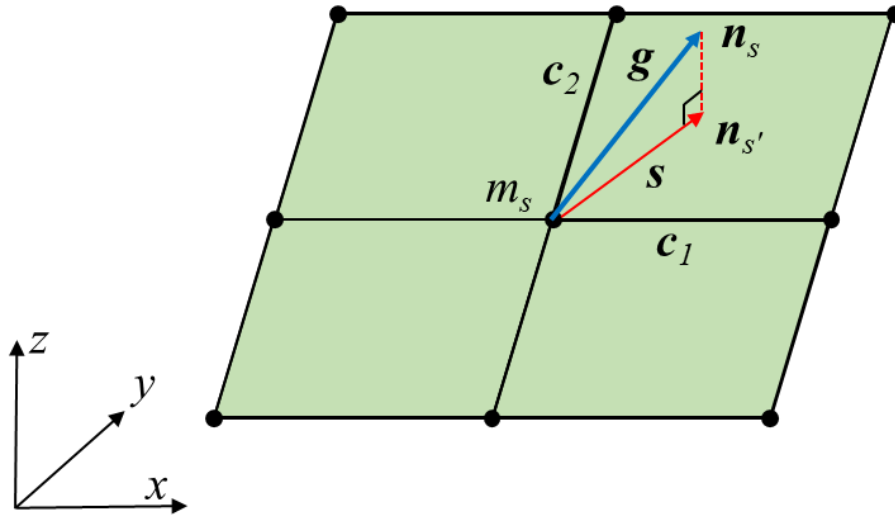


Fig.5. The projection of the vector g onto the principal segment.

After establishing a list of contact neighbors on the surface, the point-to-surface contact search algorithm determines the true contact state between material points and contact surfaces. As shown in Fig. 5, for the position between a main segment centered from point n_s to m_s on the main plane, the projection point of the slave point on the main segment is located in the main segment, and the gap value from the point to the main segment is less than 0.5Δ , if the position between the slave point and the main segment is satisfied. The slave point is considered to be a real contact pair with the main segment in the current time step, and the contact force generated by the slave point is calculated using the penalty function method. Otherwise, it is considered that there is no contact between the slave point and the master segment in the current time step.

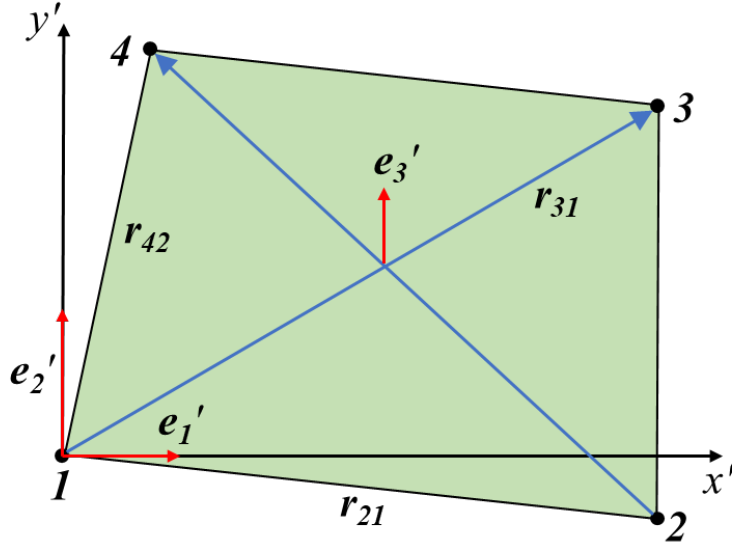


Fig.6. The projection plane constructed.

For the calculation of projection points from the point to the main segment [49], both the point and the main segment are projected onto a plane, and the three-dimensional space problem is transformed into a two-dimensional plane problem. The structure of the projection plane is shown in Fig. 6. The base vector of the projection plane can be expressed as:

$$\begin{aligned} \mathbf{e}_3' &= \frac{\mathbf{r}_{31} \times \mathbf{r}_{42}}{\|\mathbf{r}_{31} \times \mathbf{r}_{42}\|} \\ \mathbf{e}_1' &= \frac{\mathbf{r}_{21} - (\mathbf{r}_{21} \cdot \mathbf{e}_3') \mathbf{e}_3'}{\|\mathbf{r}_{21} - (\mathbf{r}_{21} \cdot \mathbf{e}_3') \mathbf{e}_3'\|} \\ \mathbf{e}_2' &= \mathbf{e}_3' \times \mathbf{e}_1' \end{aligned} \quad (18)$$

Suppose that the coordinates of the slave point on the projector plane are (x', y') , and the coordinates of the point on the main segment on the projector plane are (x_i', y_i') , $(i = 1 \sim 4)$. A bilinear interpolation function is used to describe the main segment, and local coordinates (r, t) are constructed. If the slave point is in the main segment, the coordinates of the slave point can be expressed as

$$\begin{cases} x' = \sum_{i=1}^4 N_i(r, t) x_i' \\ y' = \sum_{i=1}^4 N_i(r, t) y_i' \end{cases} \quad (19)$$

$$N_i(r, t) = \frac{1}{4} (1 + r_i r) (1 + t_i t) \quad (20)$$

where: (r, t) is the local coordinate of the slave point, and (r_i, t_i) is the local coordinate of the i th point in the main segment. Based on Eq. (19), Eq. (20) the value of the local coordinate (r, t) of the point can be calculated. If the calculated local coordinates r and t of the slave point are in the interval $[-1, 1]$, then the projection of the slave point to the main segment is inside the main segment. The distance from the point to the main segment can be calculated by projecting the local coordinates (r, t) from the point onto the main segment:

$$\boldsymbol{\delta}_p = [\mathbf{x}^s - \mathbf{x}_c(r, t)] \cdot \mathbf{n}^m \quad (21)$$

where: \mathbf{x}^s is the coordinate of the slave point; \mathbf{x}_c is the coordinates of the contact point (projection point); \mathbf{n}^m is the normal vector for the primary segment.

The following steps are taken to implement the algorithm:

1. A contact neighbors list is constructed for the surface by using the Verlet neighbor list of particles;

2. Then a projection surface is constructed by using Eq. (18) to transform the three-dimensional space problem into a two-dimensional plane problem;
3. Bilinear interpolation functions are used to describe points on the surface;
4. The particles from the surface contact neighbor list are projected to the projection surface, assuming that the projection point is located inside the main segment, and represent the position of the projection point through an interpolation function, denoted as (r, t) ;
5. If the calculated local coordinates r and t of the slave point are in the interval $[-1, 1]$, the particle's projection is inside the main segment, and the distance between the point and the main segment is calculated using Eq. (21); Otherwise, the projection of the particle is not within the main segment, and the surface continues to loop to the next particle in the surface contact neighbor list.

2.2.4. Contact Force

The penalty function method [50, 51] is used to calculate the contact force between contact pairs. The classical Hertz law relates the contact force to a nonlinear power function of penetration depth, which can be expressed as:

$$F_N = K\delta_p^n \quad (22)$$

where δ_p represents the relative penetration depth between the contacts, n is nonlinear power exponents and K is the contact stiffness parameter determined by the material and geometric properties of the local region of the contact body. Here, the contact is considered to be a point-to-surface contact problem between a point and a plane of a substance. The expression for the contact stiffness [52] is:

$$K = \frac{4}{3(m_i + m_j)} \sqrt{R_i} \quad (23)$$

where material parameters m_i and m_j are given by the following formula

$$m_l = \frac{1 - \nu_l^2}{E_l}, \quad (l = i, j) \quad (24)$$

where, ν_l and E_l are the Poisson's ratio and elastic modulus of the two contact objects respectively. After calculating the contact force of the material point through the penalty function, the acceleration of the point is calculated by considering the internal force, external force, and contact force of the material point.

2.3. Numerical Implementation

Here, the theoretical formula of PD and proposed contact algorithm are introduced. For the contact calculation in this study, geometric models need to be constructed first, including reading particle information, material properties, and material properties. Then the initial conditions, including particle velocity $\dot{\mathbf{u}}$, displacement \mathbf{u} and external volume force \mathbf{b} , etc are considered. Finally the solution information, including the calculation time step Δt , the solution time, and the output time interval are determined. The equation of motion of PD based on bonds under spatial dispersion is as follows:

$$\rho_i \ddot{\mathbf{u}}_i^n = \sum_j \mathbf{f}(\mathbf{u}_j^n - \mathbf{u}_i^n, \mathbf{x}_j - \mathbf{x}_i) V_j + \mathbf{b}_i^n \quad (25)$$

where n is the iteration time step, subscript i, j is the number of material point, V_j denotes the volume occupied by material point j , \mathbf{f} is the bond pair force, which can be expressed as:

$$\mathbf{f}(\mathbf{u}_j^n - \mathbf{u}_i^n, \mathbf{x}_j - \mathbf{x}_i) = cs_{ij}^n \mathbf{n}_{ij}^n \quad (26)$$

where s_{ij}^n represents the relative elongation between material point i and j bond pairs at the n th time step, and \mathbf{n}_{ij}^n is the unit vector between material point i and j bond pairs at the n th time step.

Since the motion equation of PD is a dynamic equation that includes an inertial term. To solve quasi-static contact problems, it is necessary to perform special processing on the motion equation to quickly converge the calculation results to static conditions. The commonly used method is the

Adaptive Dynamic Relaxation (ADR) [53, 54]. This method artificially increases damping by introducing new fictitious inertia and damping terms into the PD motion equation to calculate the optimal damping coefficient for each time step. The motion equation containing damping terms is written as:

$$\mathbf{D}\ddot{\mathbf{U}}(\mathbf{X}, t) + c\mathbf{D}\dot{\mathbf{U}}(\mathbf{X}, t) = \mathbf{F}(\mathbf{U}, \mathbf{U}', \mathbf{X}, \mathbf{X}') \quad (27)$$

where \mathbf{D} is the fictitious diagonal density matrix and c is the damping coefficient determined by Rayleigh's quotient. Furthermore, the vectors \mathbf{U} and \mathbf{X} represent displacements and positions at the collocation points. The vector \mathbf{F} is the summation of internal and external forces and its i th component can be written as

$$\mathbf{F}_i = \sum_{j=1}^N [\mathbf{f}(\mathbf{u}_j - \mathbf{u}_i, \mathbf{x}_j - \mathbf{x}_i)] [v_{c(j)} V_j] + \mathbf{b}(\mathbf{x}_j) \quad (28)$$

By utilizing central-difference explicit integration, displacements and velocities for the next time step can be obtained as

$$\dot{\mathbf{U}}^{n+1/2} = \frac{((2+c^n\Delta t)\dot{\mathbf{U}}^{n-1/2} + 2\Delta t\mathbf{D}^{-1}\mathbf{F}^n)}{(2+c^n\Delta t)} \quad (29)$$

$$\mathbf{U}^{n+1} = \mathbf{U}^n + \Delta t\dot{\mathbf{U}}^{n+1/2}$$

where n indicates the n^{th} iteration. The time integration at the initial moment can be expressed by the following equation:

$$\dot{\mathbf{U}}^{1/2} = \frac{\Delta t\mathbf{D}^{-1}\mathbf{F}^0}{2} \quad (30)$$

To ensure the stability of the calculation, the diagonal elements of the density matrix, \mathbf{D} , can be expressed as

$$\lambda_{ii} \geq \frac{\Delta t^2}{4} \sum_j |K_{ij}| \quad (31)$$

in which K_{ij} is the stiffness matrix of the system under consideration. The damping coefficient can be determined by using the lowest frequency of the system.

$$c^n = 2\sqrt{((\mathbf{U}^n)^T {}^1\mathbf{K}^n \mathbf{U}^n) / ((\mathbf{U}^n)^T \mathbf{U}^n)} \quad (32)$$

in which ${}^1\mathbf{K}^n$ is the diagonal "local" stiffness matrix, which can be expressed as

$${}^1\mathbf{K}^n = -(F_i^n / \lambda_{ii} - F_i^{n-1} / \lambda_{ii}) / (\Delta t \dot{u}_i^{n-1/2}) \quad (33)$$

The total flowchart of the program is shown in Fig. 7. As PD is a complicated mesh-free method without any grid, we use commercial software ANSYS to model the model, export node and element information, and create input files to read and model in the PD program.

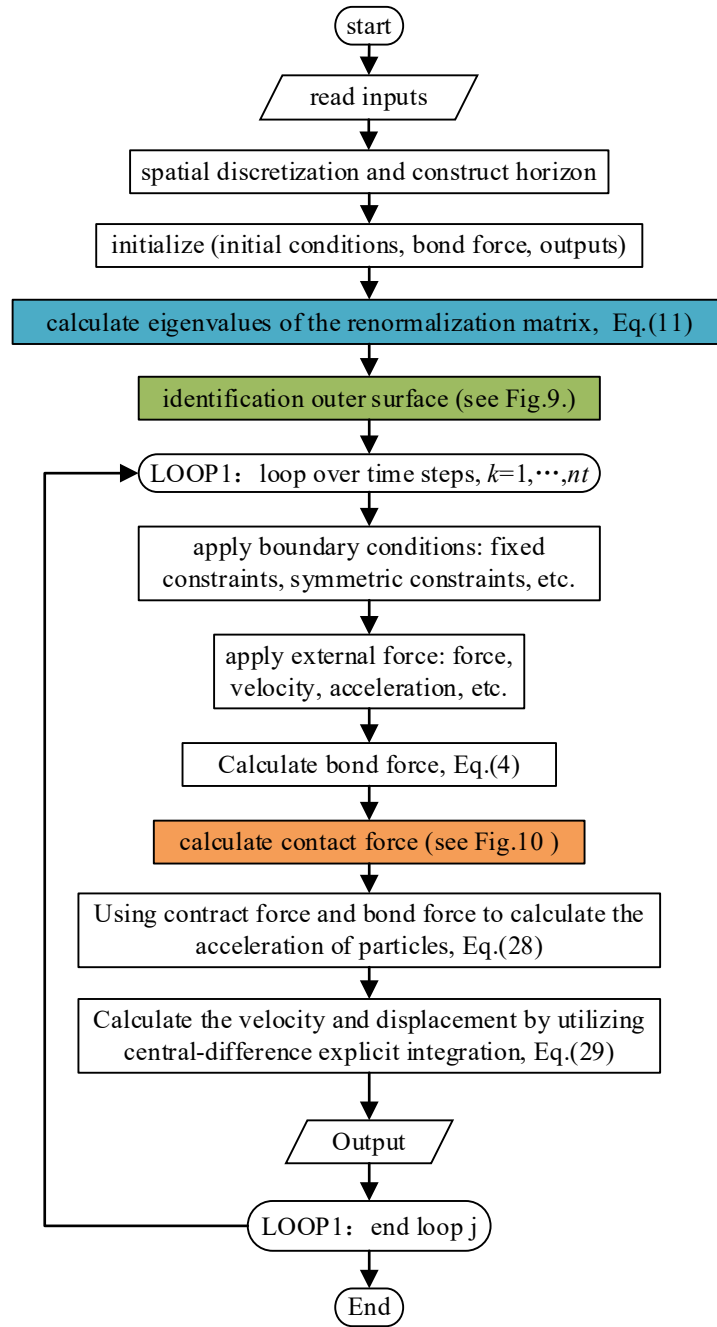


Fig.7. Flowchart of total algorithm.

Therefore, the search for the outer surface mainly searches the element faces in the imported element information, which is not used in calculating bond forces in PD programs. The flowchart for searching the face of elements is shown in Fig. 8. We use the eigenvalue method to identify the particles on the surface of the model. The identification process diagram for outer surface particles is shown in Fig. 9.

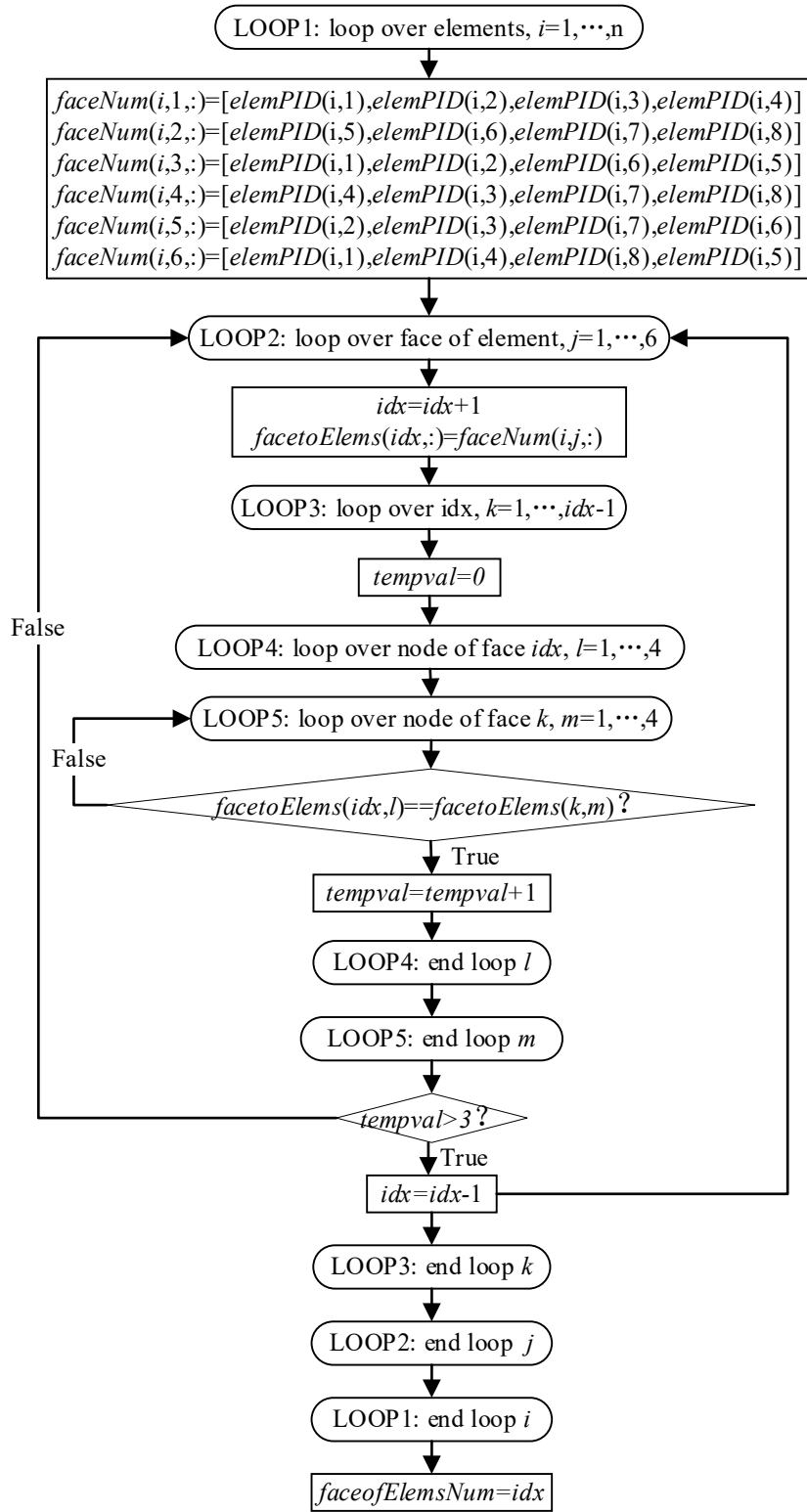


Fig.8. Flowchart for recognizing the face of elements.

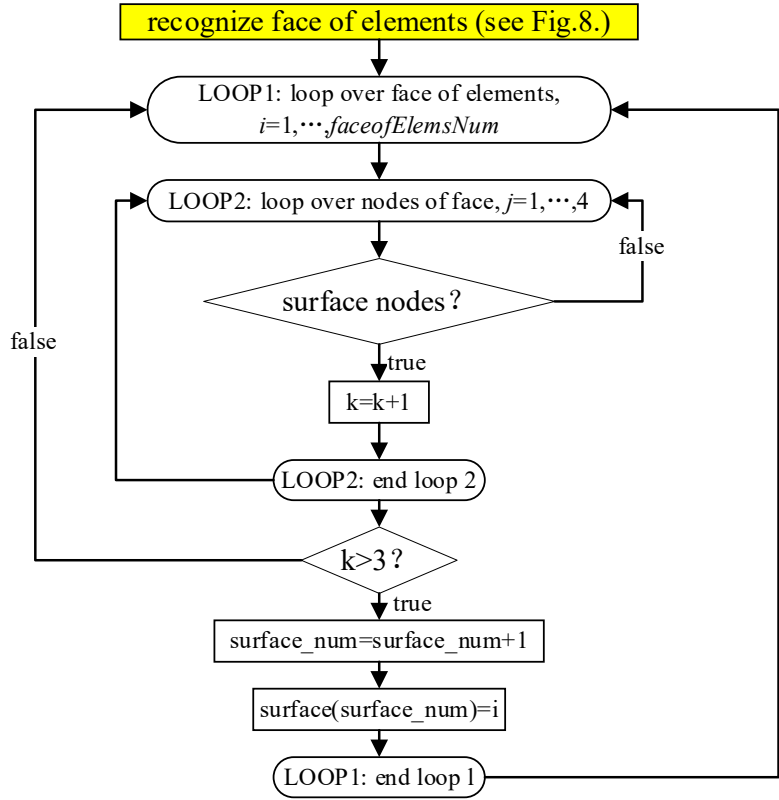


Fig.9. Flowchart for recognizing surface.

Then by updating the Verlet neighbors list of surface particles, the contact pairs that may have contact are pre-searched. The contact neighbors list of the contact surface is established by the union of Verlet neighbors list of the four points on the surface. Next, the detailed location information of possible contact pairs is obtained by the point-to-surface contact search algorithm. Finally, the contact force for determining the position information of the contact pair is calculated using the penalty function method. The detailed calculation flowchart is shown in Fig. 10.

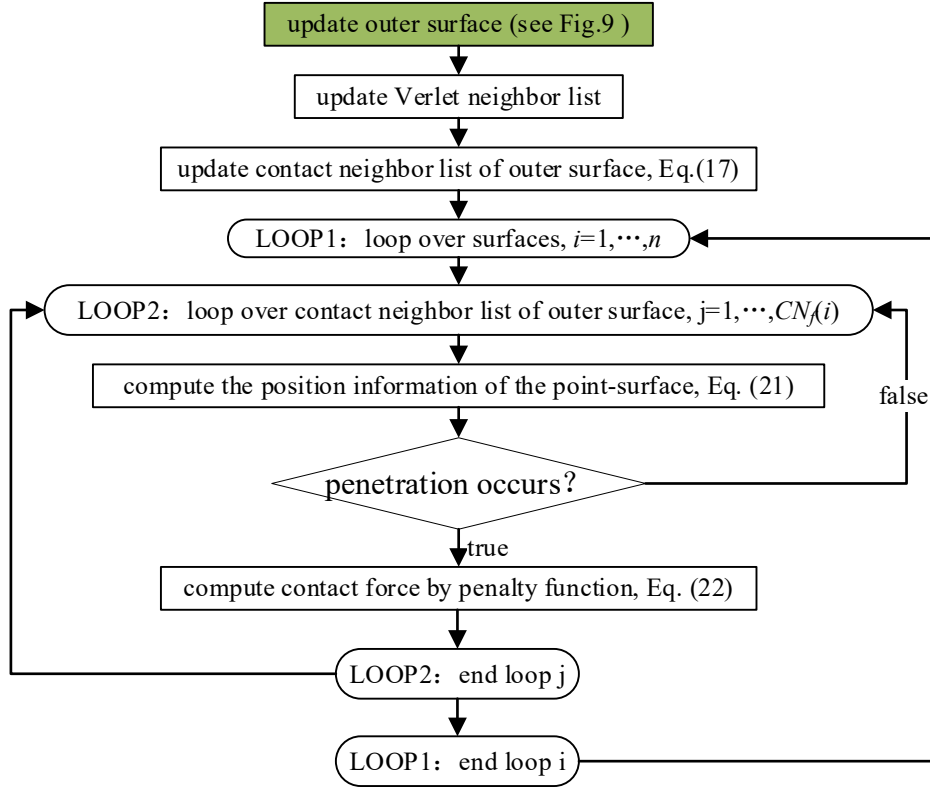


Fig.10. Flowchart of contact algorithm.

3. Verification of Model

In the present study, the contact process of elastic and rigid bodies is studied using the proposed contact algorithm. First, the accuracy of the model is verified by comparing the contact force obtained from the contact calculation of an elastic sphere with a rigid body plane with the theoretical value. The effects of discrete parameters, and unit time step on the simulation results are also analyzed. In addition, the contact model of elastic roller and rigid plane, and the model of rigid punch and elastic half-space were examined respectively. the estimated contact forces are compared and analyzed with the theoretical values in Hertz contact theory [55].

3.1. Elastic Sphere Contact

In Hertz contact theory [55], for the contact problem between a smooth and frictionless elastic sphere and a plane, the sphere is subjected to a downward external force P , which contacts the plane and forms a contact circle with a radius of a , as shown in Fig. 11. And the pressure on the contact surface between the sphere and the plane has a parabolic relationship with the contact radius, expressed as

$$p(x) = p_0 \left[1 - \left(\frac{x}{a} \right)^2 \right]^{1/2} \quad (34)$$

Among them, the expressions for contact radius a , maximum pressure p_0 , and average pressure p_m are respectively.

$$a = \left(\frac{3PR}{4E'} \right)^{1/3} \quad (35)$$

$$p_0 = \frac{3P}{2\pi a^2} \quad (36)$$

$$p_m = \frac{P}{\pi a^2} = \frac{2}{3}p_0 \quad (37)$$

$$E' = \left(\frac{1-\nu_1^2}{E_1} + \frac{1-\nu_2^2}{E_2} \right)^{-1} \quad (38)$$

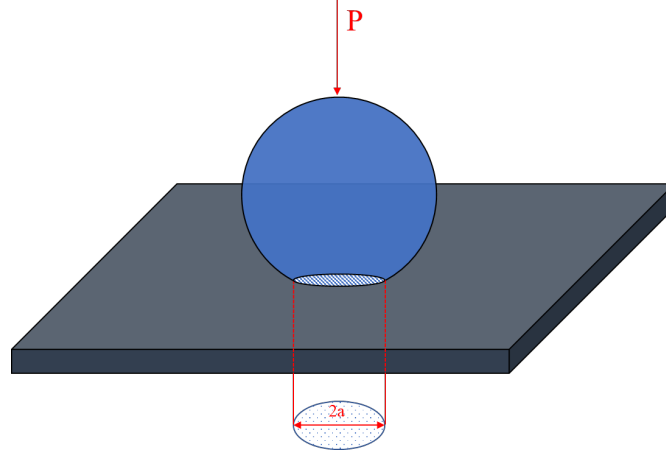


Fig.11. Diagram of elastic sphere contact.

According to the above benchmark calculation example, the contact model between a purely elastic sphere and a rigid plane is constructed with a sphere radius of 1m. The density, elastic modulus, and Poisson's ratio are 1000kg/m^3 , 1GPa , and 0.25 , respectively.

The sphere is modeled by a PD composition based on linear elastic bonds, while the plane is considered to be rigid without any deformation. The model is shown in Fig. 12. The grid size of the model is 0.08m and the horizon size of the particle is scaled to 3 times the grid size. Then the eigenvalue method introduced in Section 2.2.1 is used to recognize the outer surface particles, as shown in Eq. (15), when the value of the minimum eigenvalue λ is greater than 0.75 , the material particle i is considered to be an internal particle; otherwise, the material point i is the particle on the surface [43, 23], and the recognition results are shown in Fig. 13. Later, a downward external force \mathbf{P} of magnitude $8 \times 10^8 \text{N}$ is applied to the sphere. The sphere is subjected to the downward force and acts on the rigid surface, making contact and deforming the plane. The normal pressure distribution on the contact surface satisfies the form of Eq. (34).

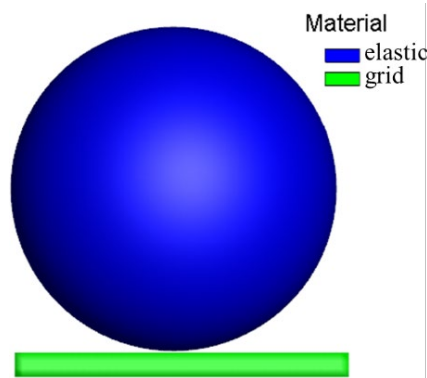


Fig.12. Elastic sphere and plane contact model.

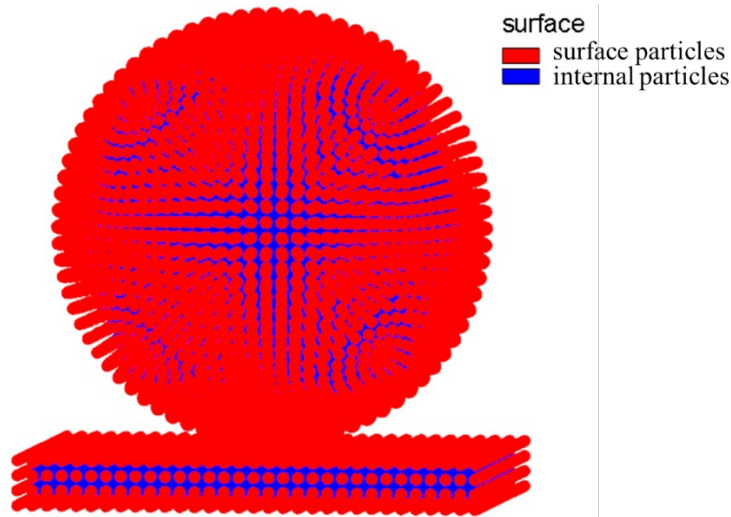


Fig.13. Searching for surface particles.

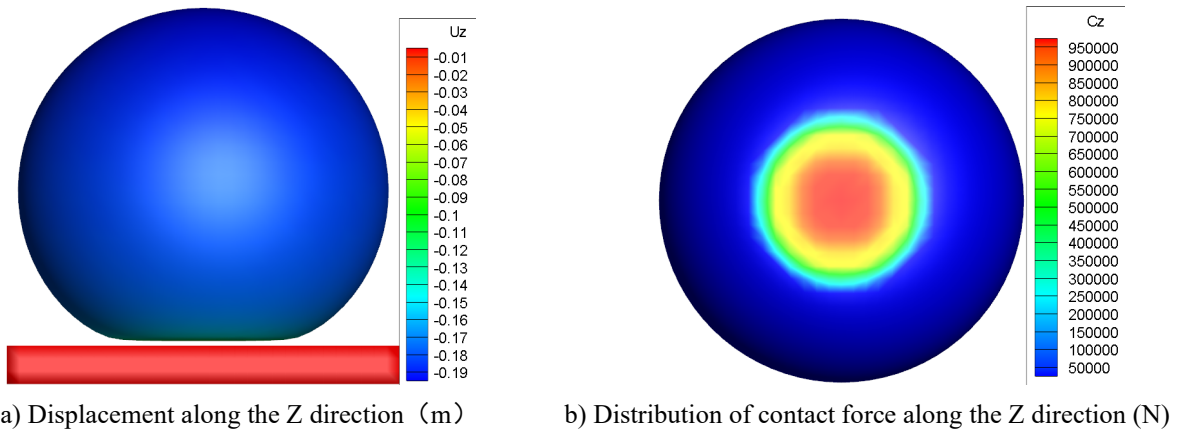


Fig.14. Displacement and force of contact between elastic sphere and plane.

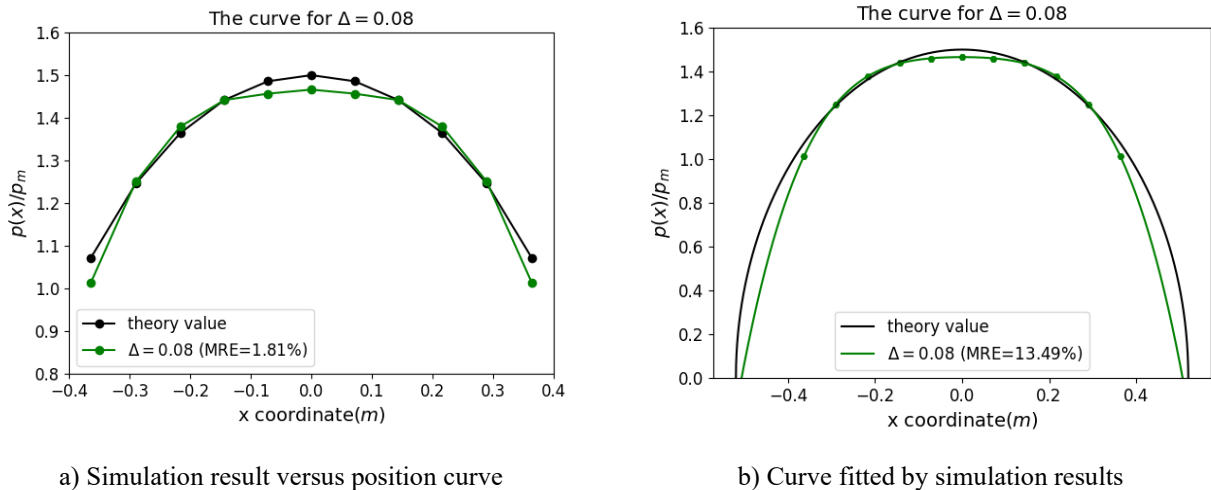


Fig.15. Contact force curve with position.

As shown in Fig. 14, when the elastic sphere is loaded downward, the elastic sphere will contact with the rigid plane and form a circular contact area. According to Eq. (35) and Eq. (36), the theoretical values of the contact radius and the maximum contact stress can be calculated as 0.52002m and

1.76563×10⁸Pa, respectively. The value of $p(x)/p_m$ of the particles on the surface of the sphere with the position curve as shown in Fig. 15 (a), by comparing the data of the particles with the curve of the theoretical value, it suggests that the mean relative error (MRE) of the contact algorithm constructed is only 1.81%, validating the accuracy of our proposed contact force algorithm. The subsequent fitting for the simulation results is shown in Fig. 15 (b). it suggests that the MRE with the theoretical results is 13.49%, and the contact radius size obtained by fitting is about 0.51m with the relative error compared to the theoretical value by about 1.92%.

3.2. Convergence Analysis

Based on the contact between an elastic sphere and a rigid plane, the effects of different neighborhood horizon size, grid size and calculate time step on the accuracy of the contact model are discussed. In the PD theory, the model is highly sensitive to grid size and neighborhood horizon size. In order to study the effect of grid size on the numerical calculations, four different grid sizes are chosen in this section: $\Delta=0.12\text{m}$, 0.08m , 0.06m and 0.04m , and the size of the neighborhood horizon is chosen to be the 8th nearest neighbor ($\sqrt{9}\Delta$). The normal phase pressure distribution curves calculated with different grid sizes are shown in Fig. 16. The results suggest that when the neighborhood horizon size is chosen the 8th nearest neighbor ($\sqrt{9}\Delta$), the effect of different grid sizes on the simulation results was investigated. And the simulation results show that, with the gradual decrease of the grid size, the simulation results are in good agreement with the theoretical values, and when the model grid size $\Delta=0.04\text{m}$, the MRE of the curves is minimized to only 7.2%.

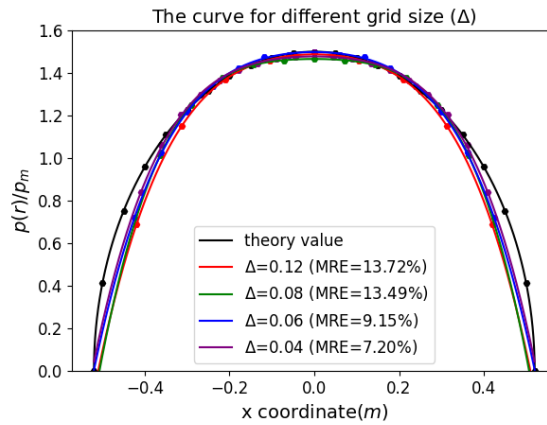
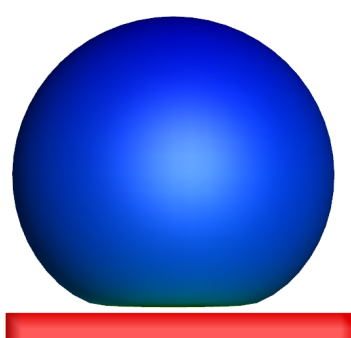
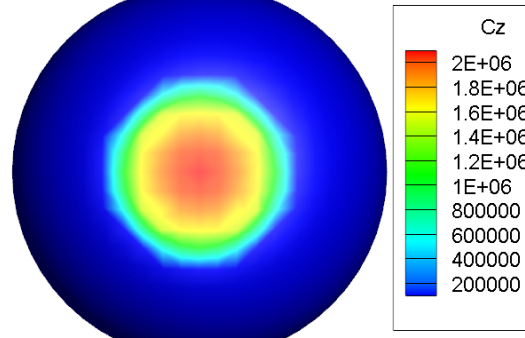
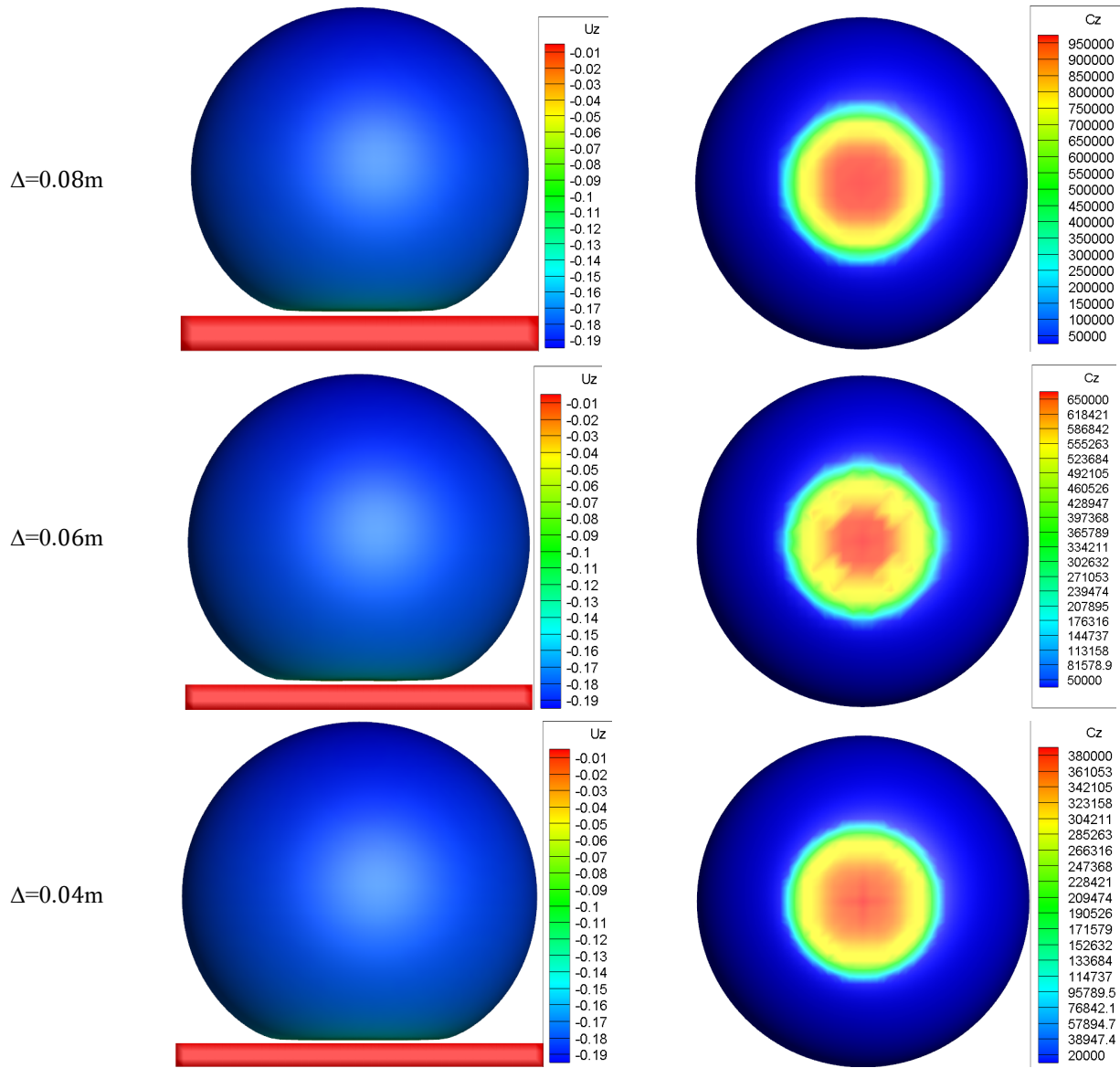


Fig.16. Contact force curve with position for different grid sizes.

Table 1 Displacement and force of contact between elastic sphere and plane for different grid sizes.

Grid size	Displacement (m)	Contact force (N)
$\Delta=0.12\text{m}$		



Meanwhile, to study the effect of different neighborhood horizon sizes on the numerical calculations, the grid size of the model $\Delta=0.08\text{m}$, and the neighborhood horizon sizes were chosen as the 7th nearest neighbor ($\sqrt{8}\Delta$), 8th nearest neighbor ($\sqrt{9}\Delta$), 9th nearest neighbor ($\sqrt{10}\Delta$), and 10th nearest neighbor ($\sqrt{13}\Delta$) in that order. The normal-phase pressure distribution curves calculated for different neighborhood horizon sizes are shown in Fig. 17. The results suggest that when the grid size of the model is chosen $\Delta=0.08\text{m}$, the effect of choosing different neighborhood horizon size on the simulation results is analyzed. The simulation results gradually tend to be close to the theoretical values when the selected neighborhood horizon size is gradually increased. When the 10th nearest neighbor ($\sqrt{13}\Delta$) is selected for the horizon size, the simulation results are in the best agreement with the theoretical values, and the MRE of the curve is only 6.77%.

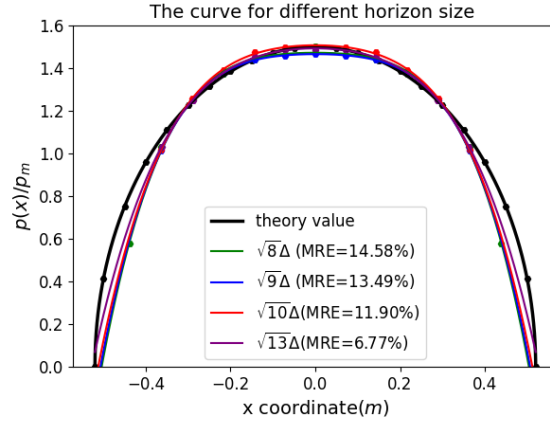


Fig.17. Contact force curve with position for different horizon sizes.

Since the contact collision problem occurs in a very short period of time we also examine the effect of time intervals on numerical calculations. three kinds of time intervals, 1×10^{-5} s, 5×10^{-6} s, and 1×10^{-6} s, are considered. The elastic sphere and plane contact model described above is selected for the model, and the grid size is $\Delta=0.08$ m, and neighborhood horizon is chosen to be three times the grid ($\sqrt{9}\Delta$). Compare the impact of different time intervals on simulation accuracy. The curve of the contact pressure on the surface of an elastic sphere with respect to its position is shown in Fig. 18. The results suggest that the simulated curves are the same for different calculation time steps, which indicates that the contact model proposed in this paper is independent of the calculation time step and depends only on the material itself.

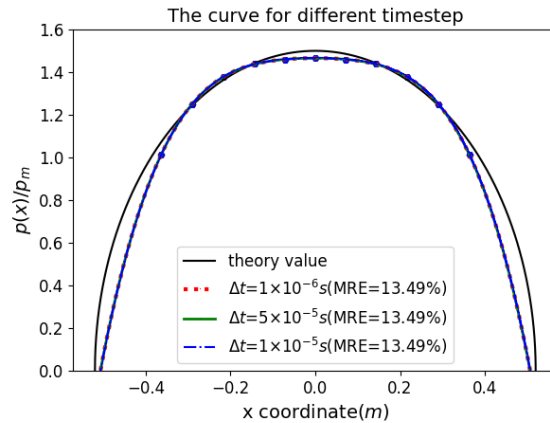


Fig.18. Contact force curve with position for different time steps.

The convergence analysis of the contact model investigates the effects of different grid size, neighborhood horizon size, and time step on the simulation accuracy. The results show that the smaller the grid size and the larger the neighborhood horizon size of the model the better the simulation results match the theoretical values. While the time step has no effect on the simulation results, the contact stiffness used in this paper is independent of the calculation time step and depends only on the material itself.

3.3. Elastic Roller Contact

Herein, the contact model simulates the contact problem between the elastic roller and rigid plane. In Hertz contact theory [55], for the contact problem between a smooth and frictionless elastic roller

and a plane, the roller is subjected to a downward external force P , which contacts the plane and forms a rectangular surface with a contact half-width of a , as shown in Fig. 19. The pressure on the contact surface between the roller and the plane exhibits a parabolic relationship with the contact half-width, as shown in Fig. 20, it is expressed as

$$p(x) = p_0 \left[1 - \left(\frac{x}{a} \right)^2 \right]^{1/2} \quad (39)$$

where, the expressions of contact radius a , maximum pressure p_0 and average pressure p_m are respectively:

$$a = \left(\frac{4PR}{\pi E'} \right)^{1/2} \quad (40)$$

$$p_0 = \frac{2P}{\pi a} \quad (41)$$

$$p_m = \frac{P}{2a} = \frac{\pi}{4} p_0 \quad (42)$$

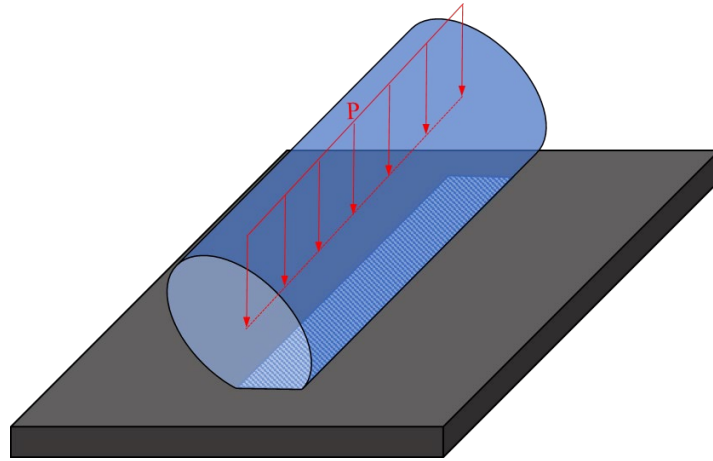


Fig.19. Diagram of elastic roller contact.

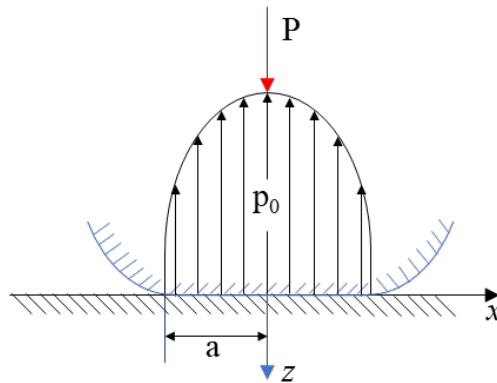


Fig.20. Schematic diagram of contact pressure distribution of elastic rollers.

Here, we construct a contact model between a pure elastic roller and a rigid plane with a radius of 1m, a length of 4m, a density of 1000kg/m^3 , and an elastic modulus of 1GPa. The roller selects the linear elastic bond-based PD constitutive model, and the plane is considered rigid without any deformation. The grid size of the model $\Delta=0.08\text{m}$, and the size of the neighborhood horizon is chosen to be the 8th nearest neighbor ($\sqrt{9}\Delta$). The model is shown in Fig. 21. Apply a downward external force $P = 8 \times 10^8 \text{N/m}$ to the roller. The roller is subjected to a downward force and acts on a rigid

surface, causing contact and deformation with the plane. When the contact force and external force P reach equilibrium. The normal phase pressure distribution on the contact surface satisfies the form expressed in Eq. (39). The simulation results are shown in Fig. 22. Compare the contact reaction force on particles located in the middle layer $Y = 2$ along the axial direction with the theoretical value obtained from Eq. (39), as shown in Fig. 23.

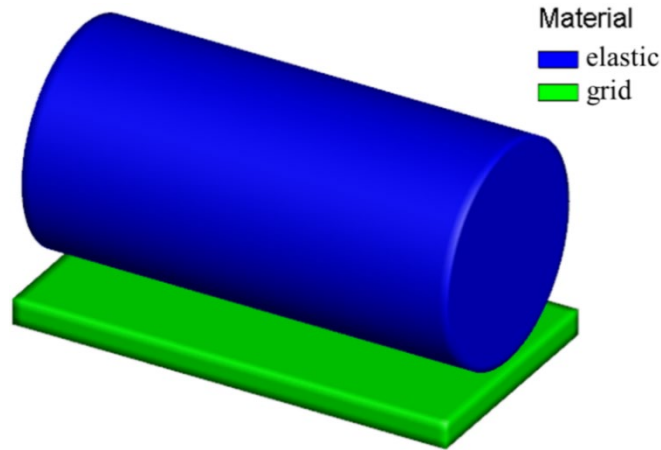
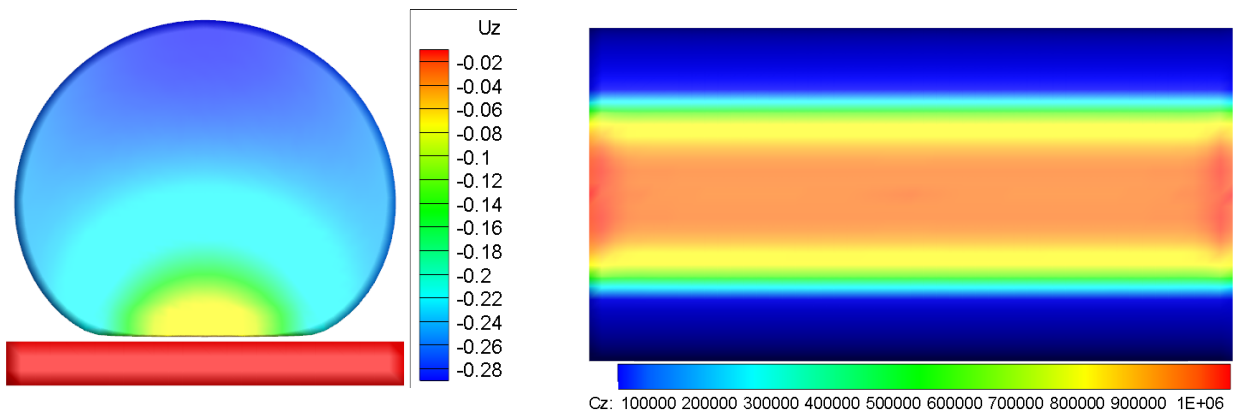


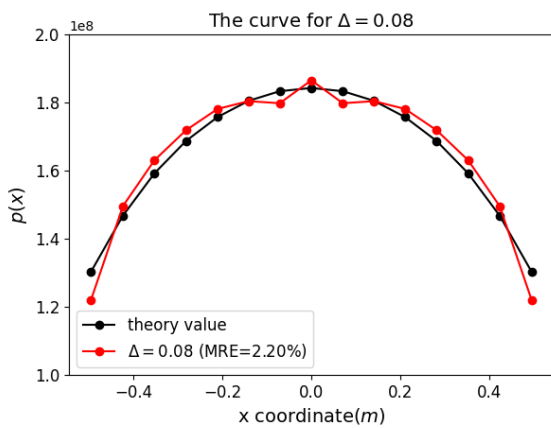
Fig.21. Elastic roller and plane contact model.



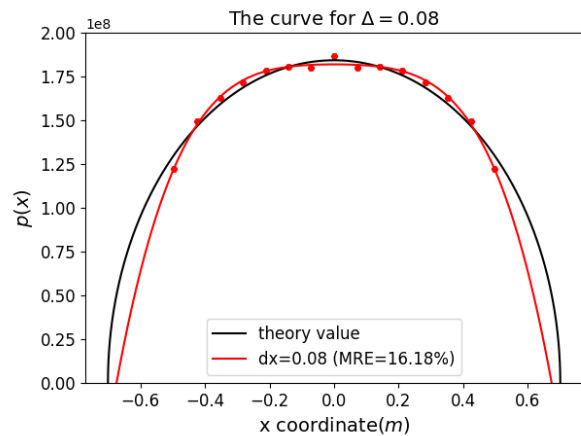
a) Displacement along the Z direction (m)

b) Distribution of contact force along the Z direction (N)

Fig.22. Displacement and force of contact between elastic roller and plane.



a) Simulation result versus position curve



b) Curve fitted by simulation results

Fig.23. Contact force curve with position.

From Fig. 19, it can be seen that when the elastic roller is subjected to a downward linear load, it will contact with the rigid plane and form a rectangular contact area. According to Eq. (40) and Eq. (41), the theoretical values of the contact radius and the maximum contact stress are 0.69099m and $1.84264 \times 10^8 \text{Pa}$, respectively. The change of the contact force of the particles on the outer surface of the roller with respect to the position is shown in Fig. 23 (a). The result suggests that the MRE of contact force between contact algorithm and theoretical value is only 2.2%, indicating well consistent with theoretical value. Then, the simulation results are curve-fitted and compared with the theoretical values, as shown in Fig. 23 (b). From the fitting results, it can be found that the MRE with the theoretical results at this time is 16.18%, and the contact radius size obtained by fitting is about 0.671m, and the relative error with the theoretical value is about 2.89%.

3.4. Rigid Punch Contact

Regarding the contact problem between an elastic half-space and a rigid punch. In Hertz contact theory [55], for the contact problem between a smooth and frictionless elastic half-space and a rigid punch, the punch has a flat base of width $2a$ and has sharp corners, the punch is subjected to a downward external force P , as shown in Fig. 24, the positional relationship between the punch and the pressure on the plane with the change of position can be expressed as:

$$p(x) = \frac{P}{\pi(a^2 - x^2)^{1/2}} \quad (43)$$

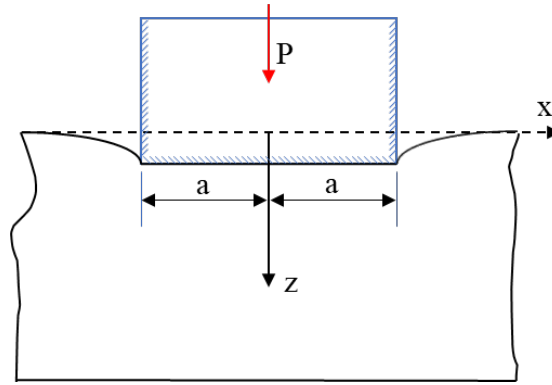


Fig.24. Schematic diagram of contact between rigid punch and elastic half-space.

Based on the benchmark calculation example mentioned above, the contact model between the elastic half-space and the rigid punch is constructed, the length of the punch is 5m, the density is 1000kg/m^3 , and the punch is considered rigid without any deformation, the elastic half-space is selected to be modeled by a PD composition based on linear elastic bonds, and the density, the elastic modulus, and the Poisson's ratio are 1000kg/m^3 , 1GPa, and 0.25, respectively. The grid size of the model $\Delta=0.08\text{m}$, and the size of the neighborhood horizon is chosen to be the 8th nearest neighbor ($\sqrt{9}\Delta$). The model is shown in Fig. 25. A downward external force $P = 8 \times 10^8 \text{N/m}$ is applied to the punch. The punch is subjected to a downward force and acts on the elastic half-space to produce contact and deformation. When the contact force and the external force P reach equilibrium. The normal phase pressure distribution on the contact surface satisfies the form of Eq. (44).

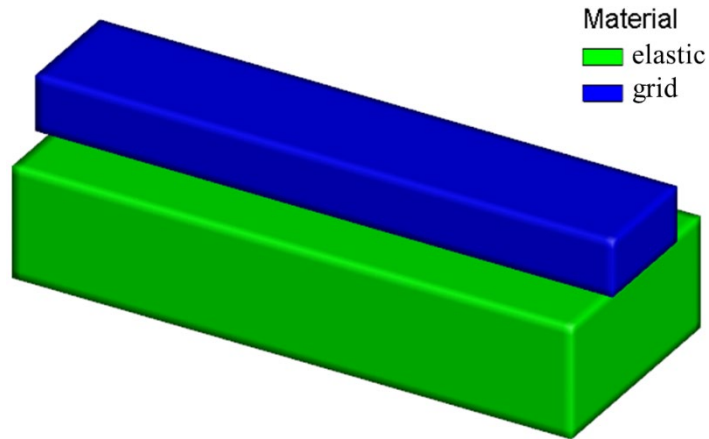
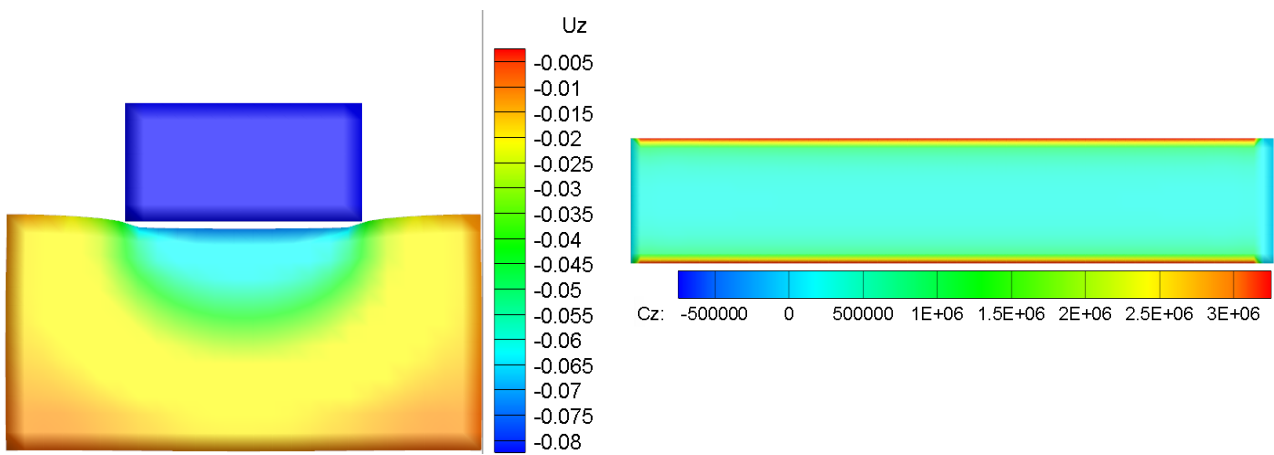


Fig.25. Rigid punch and elastic half-space model.



a) Displacement along the Z direction (m)

b) Distribution of contact force along the Z direction (N)

Fig.26. Displacement and force of contact between rigid punch and elastic half-space.

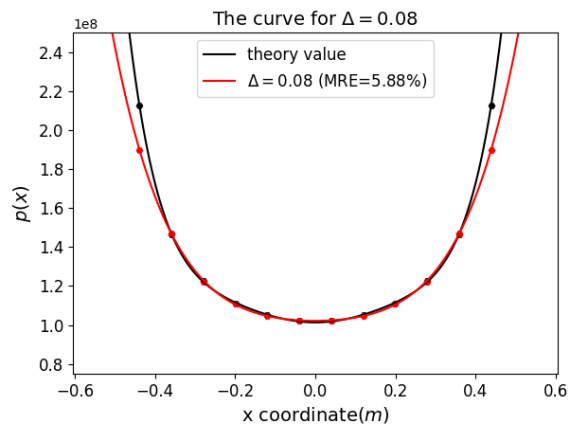


Fig.27. Contact force curve with position.

The simulation results are shown in Fig. 26. The contact force on the punches located on the contact surface is then compared with the theoretical value derived from Eq. (44) as shown in Fig. 27. From the results, it can be observed that the average relative error between the modeled contact force profile and the theoretical value is only 5.88%.

4. Conclusion

In the present study, we proposed an improved point-to-surface contact model in PD with high accuracy. The eigenvalue method is first used to identify the particles on the model surface. Then to improve the computational efficiency, we establish the Verlet list to globally search for possible contact positions, effectively identifying potential contact pairs. Subsequently, a list of contact neighbors of the surface is constructed by identifying the surface particles and the outer surface. Next, the point-to-surface contact algorithm is used to calculate the position of the contact pair. The contact force of the contact pair is calculated by the penalty function method. Finally, by simulating several representative contact experiments, the simulated contact forces on the contact surfaces are in good agreement with the theoretical values, validating the accuracy of our proposed contact model. Particularly, by identifying the surface particles, the contact model can automatically identify and calculate the contact force for the outer surface of the model, which promote the development of contact algorithms in PD and other meshfree methods.

5. References

- [1] Silling S A. Reformulation of elasticity theory for discontinuities and long-range forces[J]. *Journal of the Mechanics and Physics of Solids*, 2000, 48(1): 175-209.
- [2] Silling S A, Epton M, Weckner O, et al. Peridynamic states and constitutive modeling[J]. *Journal of Elasticity*, 2007, 88(2): 151-184.
- [3] Silling S A. Linearized theory of peridynamic states[J]. *Journal of Elasticity*, 2010, 99(1): 85-111.
- [4] Wang X, Dong W, He Q, et al. Nonlocal thermomechanical coupled analysis of wheel-rail contact using a peridynamic model[J]. *Wear*, 2023, 528-529: 204954.
- [5] Wu L, Wang L, Huang D, et al. An ordinary state-based peridynamic modeling for dynamic fracture of laminated glass under low-velocity impact[J]. *Composite Structures*, 2020, 234: 111722.
- [6] Silling S A, Askari E. A meshfree method based on the peridynamic model of solid mechanics[J]. *Computers and Structures*, 2005, 83(17-18): 1526-1535.
- [7] Zhang Y, Tao L, Ye L, et al. An updated fast continuous contact detection algorithm and its implementation in case study of ice-structure interaction by peridynamics[J]. *Marine Structures*, 2023, 89: 103406.
- [8] Isiet M, Mišković I, Mišković S. Review of peridynamic modelling of material failure and damage due to impact[M]//*International Journal of Impact Engineering*. Pergamon, 2021: 103740.
- [9] Guan J, Yan X, Guo L. An adaptive contact model involving friction based on peridynamics[J]. *European Journal of Mechanics, A/Solids*, 2023, 100: 104966.
- [10] Sachdeva T D, Ramakrishnan C V. A finite element solution for the two-dimensional elastic contact problems with friction[J]. *International Journal for Numerical Methods in Engineering*, 1981, 17(8): 1257-1271.
- [11] Chabrand P, Dubois F, Raous M. Various numerical methods for solving unilateral contact problems with friction[J]. *Mathematical and Computer Modelling*, 1998, 28(4-8): 97-108.
- [12] Li Y, Zhang G Y, Liu G R, et al. A contact analysis approach based on linear complementarity formulation using smoothed finite element methods[J]. *Engineering Analysis with Boundary Elements*, 2013, 37(10): 1244-1258.
- [13] Chan S K, Tuba I S. A finite element method for contact problems of solid bodies-Part I. Theory and validation[J]. *International Journal of Mechanical Sciences*, 1971, 13(7): 615-625.
- [14] Li Y, Chen Q, Feng Z. A cell-based smoothed finite element method for multi-body contact analysis within the bi-potential formulation[J]. *Engineering Analysis with Boundary Elements*, 2023, 148: 256-266.
- [15] Fang H, Yin Z Y, Peng M, et al. Improved SNS-PFEM framework with dual mortar method to model geotechnical large deformation contact problems[J]. *Computer Methods in Applied Mechanics and Engineering*, 2023, 412.
- [16] Sun C, Liu G R, Huo S H, et al. A novel node-to-segment algorithm in smoothed finite element method for contact problems[J]. *Computational Mechanics*, 2023, 72(5): 1029-1057.
- [17] Randles P W, Libersky L D. Smoothed Particle Hydrodynamics: Some recent improvements and applications[J]. *Computer Methods in Applied Mechanics and Engineering*, 1996, 139(1-4): 375-408.
- [18] Campbell J, Vignjevic R, Libersky L. A contact algorithm for smoothed particle hydrodynamics[J]. *Computer Methods in Applied Mechanics and Engineering*, 2000, 184(1): 49-65.
- [19] Zhan L, Peng C, Zhang B, et al. A SPH framework for dynamic interaction between soil and rigid body system with hybrid contact method[J]. *International Journal for Numerical and Analytical Methods in Geomechanics*, 2020, 44(10): 1446-1471.
- [20] Xiao Y, Liu K. 3D Surface-to-Surface Contact Algorithm for SPH Method and Its Application to Simulation of Impact Failure of Ceramic Plate[J]. *Applied Sciences (Switzerland)*, 2023, 13(6): 3790.
- [21] Lone A S, Kanth S A, Harmain G A, et al. Modeling of Large Sliding Between Contacting Bodies by Penalty-Based Element-Free Galerkin Method Using Node-to-Segment Approach[J]. *Iranian Journal of Science and Technology - Transactions of Mechanical Engineering*, 2023, 47(4): 1985-2002.
- [22] Dilts G A, Dilts, A. G. Moving least-squares particle hydrodynamics II: conservation and boundaries[J]. *IJNME*, 2000, 48(10): 1503-1524.
- [23] Marrone S, Colagrossi A, Le Touzé D, et al. Fast free-surface detection and level-set function definition in SPH solvers[J]. *Journal of Computational Physics*, 2010, 229(10): 3652-3663.
- [24] Liu X, Mao J, Zhao L, et al. The distance potential function-based finite-discrete element method[J]. *Computational Mechanics*, 2020, 66(6): 1477-1495.
- [25] Madenci E, Oterkus E. *Peridynamic Theory and Its Applications*[M]. New York, NY: Springer New York, 2014.
- [26] Gu X, Zhang Q, Huang D, et al. Wave dispersion analysis and simulation method for concrete SHPB test in peridynamics[J]. *Engineering Fracture Mechanics*, 2016, 160: 124-137.
- [27] Liu Y, Liu L, Mei H, et al. A modified rate-dependent peridynamic model with rotation effect for dynamic mechanical behavior of ceramic

- materials[J]. *Computer Methods in Applied Mechanics and Engineering*, 2022, 388: 114246.
- [28] Chu B, Chu B, Liu Q, et al. A rate-dependent peridynamic model for the dynamic behavior of ceramic materials[J]. *CMES - Computer Modeling in Engineering and Sciences*, 2020, 124(1): 151-178.
- [29] Macek R W, Silling S A. Peridynamics via finite element analysis[J]. *Finite Elements in Analysis and Design*, 2007, 43(15): 1169-1178.
- [30] Parks M L, Lehoucq R B, Plimpton S J, et al. Implementing peridynamics within a molecular dynamics code[J]. *Computer Physics Communications*, 2008, 179(11): 777-783.
- [31] Wang L, Yin Z Y, Chen W. Peridynamic modelling of dynamic damage and fragmentation of cracked solids during impact contact[J]. *Engineering Fracture Mechanics*, 2024, 295: 109784.
- [32] Tupek M R, Rimoli J J, Radovitzky R. An approach for incorporating classical continuum damage models in state-based peridynamics[J]. *Computer Methods in Applied Mechanics and Engineering*, 2013, 263: 20-26.
- [33] Littlewood D J. *Simulation of Dynamic Fracture Using Peridynamics, Finite Element Modeling, and Contact*[C]//Volume 9: Mechanics of Solids, Structures and Fluids: Vol. 9. ASMEDE, 2010: 209-217.
- [34] Lee J, Liu W, Hong J W. Impact fracture analysis enhanced by contact of peridynamic and finite element formulations[J]. *International Journal of Impact Engineering*, 2016, 87: 108-119.
- [35] Kamensky D, Behzadinasab M, Foster J T, et al. Peridynamic Modeling of Frictional Contact[J]. *Journal of Peridynamics and Nonlocal Modeling*, 2019, 1(2): 107-121.
- [36] Lu W, Oterkus S, Oterkus E, et al. Modelling of cracks with frictional contact based on peridynamics[J]. *Theoretical and Applied Fracture Mechanics*, 2021, 116: 103082.
- [37] Silling S A. Meshfree peridynamics for soft materials[J]. 2016(2011): 1-30.
- [38] Zhang H, Zhang X, Liu Y. A peridynamic model for contact problems involving fracture[J]. *Engineering Fracture Mechanics*, 2022, 267: 108436.
- [39] Zhao J, Lu G, Zhang Q, et al. Modelling of contact damage in brittle materials based on peridynamics[J]. *CMES - Computer Modeling in Engineering and Sciences*, 2021, 129(2): 519-539.
- [40] Le Q V, Bobaru F. Surface corrections for peridynamic models in elasticity and fracture[J]. 2018, 61: 499-518.
- [41] Oterkus E, Oterkus E. *Peridynamic Theory for Modeling Three-Dimensional Damage Growth in Metallic and Composite Structures*[D]. The University of Arizona., 2010[2024-05-20].
- [42] Madenci E, Oterkus E. *Peridynamic theory and its applications*[M]//Peridynamic Theory and Its Applications: Vol. 9781461484. 2014.
- [43] Doring M. Développement d'une méthode SPH pour les applications à surface libre en hydrodynamique[J]. 2005.
- [44] Sun P, Ming F, Zhang A. Numerical simulation of interactions between free surface and rigid body using a robust SPH method[J]. *Ocean Engineering*, 2015, 98: 32-49.
- [45] Allen M P, Tildesley D J. *Computer simulation of liquids*[J]. Clarendon Press, 1987.
- [46] Verlet L. Computer "experiments" on classical fluids. I. Thermodynamical properties of Lennard-Jones molecules[J]. *Physical Review*, 1967, 159(1): 98-103.
- [47] Lai X, Liu L, Li S, et al. A non-ordinary state-based peridynamics modeling of fractures in quasi-brittle materials[J]. *International Journal of Impact Engineering*, 2018, 111: 130-146.
- [48] Benson D J, Hallquist J O. A single surface contact algorithm for the post-buckling analysis of shell structures[J]. *Computer Methods in Applied Mechanics & Engineering*, 1990, 78(2): 141-163.
- [49] Chen C, Chen X, Liu M. Study on Erosion Contact Search Algorithms for Explicit Finite Element[J]. *Beijing Ligong Daxue Xuebao/Transaction of Beijing Institute of Technology*, 2022, 42(1): 1-10.
- [50] Hertz V H H. Die lieber die Berührung fester elastischer Körper[J]. 1878: 156-171.
- [51] Skrinjar L, Slavič J, Boltežar M. A review of continuous contact-force models in multibody dynamics[J]. *International Journal of Mechanical Sciences*, 2018, 145: 171-187.
- [52] MacHado M, Moreira P, Flores P, et al. Compliant contact force models in multibody dynamics: Evolution of the Hertz contact theory[J]. *Mechanism and Machine Theory*, 2012, 53: 99-121.
- [53] Underwood P. DYNAMIC RELAXATION.[J]. *Comput Methods for Transient Anal*, 1983: 245-265.
- [54] Kilic B, Madenci E. An adaptive dynamic relaxation method for quasi-static simulations using the peridynamic theory[J]. *Theoretical and Applied Fracture Mechanics*, 2010, 53(3): 194-204.
- [55] Johnson K L. *Contact Mechanics*[M]. American Society of Mechanical Engineers, 1985.